INORGANIC CHEMISTRY

FRONTIERS

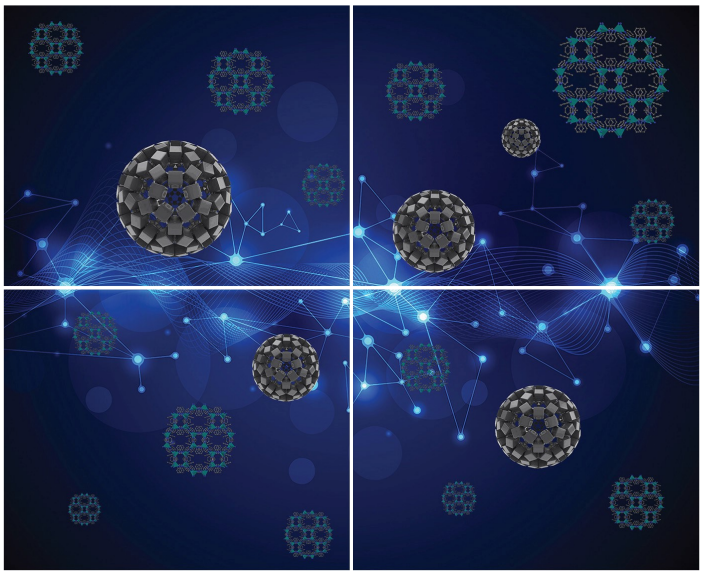

Accepted Manuscript

This article can be cited before page numbers have been issued, to do this please use: R. W. Hooper, B. Phan, T. Dey, C. Butler, D. Sarkar, C. Ni, A. Mar, J. Veinot and V. K. Michaelis, *Inorg. Chem. Front.*, 2026, DOI: 10.1039/D6QI00612D.

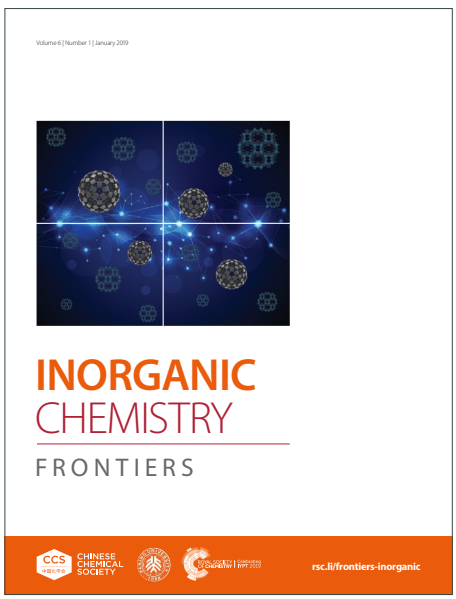

View Article Online
DOI: 10.1039/D6QI00612D

Synthetic History Matters: Understanding the Structure-Property Evolution in $CsSn_xGe_{1-x}Br_3$ Perovskites

Riley W. Hooper[1,2], Brian B. Phan[1], Trinanjan Dey[1], Cole Butler[1], Diganta Sarkar[1,3], Chuyi Ni[1], Arthur Mar[1], Jonathan G.C. Veinot[1], and Vladimir K. Michaelis[1,*]

[1]Department of Chemistry, University of Alberta, Edmonton, Alberta, Canada T6G 2G2

[2]Current address: Technical University of Munich, TUM School of Natural Sciences, Chemistry Department, Lichtenbergstraße 4, 85748 Garching bei München, Germany

[3]Current address: Université Grenoble Alpes, CEA, IRIG, MEM, Grenoble, 38000 France

*Corresponding author: vladimir.michaelis@ualberta.ca

Abstract

Metal halide perovskites and related perovskite-inspired materials continue to attract attention for next-generation photovoltaic applications. Compositional synthetic design remains the preferred method for exploring property manipulation and for gaining new insights into material stability and behaviour. This study explores the $CsSn_xGe_{1-x}Br_3$ perovskite series to elucidate how composition and preparation method, including solvent, mechanochemical, and high-temperature synthesis, direct the chemical structure and influence optoelectronic properties. Various analytical techniques, including solid-state nuclear magnetic resonance (NMR) spectroscopy, nuclear quadrupole resonance (NQR) spectroscopy, powder X-ray diffraction (XRD), diffuse reflectance spectroscopy, and electron microscopy, have been employed to characterize the local atomic environment, long-range crystallographic structure, morphology, and optical properties of the synthesized $CsSn_xGe_{1-x}Br_3$ perovskites. NMR and NQR reveal unique chemical environments and electric field gradients, and how the atomic structure responds to different synthetic conditions across the perovskite system. Paired with long-range diffraction and microscopy-based techniques, these methods provide detailed insight into crystallographic phase, B-site mixing, and domain formation across different compositions and syntheses.

View Article Online
DOI: 10.1039/D6QI00612D

Introduction

Metal halide perovskites, ABX_3 [A^+ = Cs, formamidinium (FA), methylammonium (MA); B^{2+} = Ge, Sn, Pb; X^- = Cl, Br, I], have served as promising candidates for optical applications since $MAPbI_3$ was first demonstrated to be an effective absorber layer for dye-sensitized solar cells.[1] Owing to their favourable optoelectronic properties, metal halide perovskites have naturally extended to applications in light-emitting diodes, photovoltaics, sensing, radiation detection, and lasing.[2-5] Perovskites feature a high degree of compositional tunability, high defect tolerance, and diverse and robust methods for their synthesis, enabling access to desirable semiconducting properties. The compositional and structural diversity of halide perovskites and related systems creates opportunities for property engineering through site disorder, heterovalent substitution, and the introduction of vacancies, while posing challenges for obtaining direct insight into how these structures evolve and adapt across their unique A, B, and X sites.[3, 5-17]

The lead halide perovskites are most commonly employed in perovskite solar cells, but suffer from intrinsic instability,[18-26] pose toxicity concerns,[8, 11, 17, 27] and rely on organic solvents for solution processing. In particular, hybrid lead halide perovskites are prone to degradation from moisture or heat,[18, 20, 23, 28, 29] and they exhibit structural instability arising from phase changes, segregation, and domain formation.[23, 30-34] To counteract these effects, various ion substitutions have been performed at the A and X sites[3, 4] with new emphasis on the B site by replacing Pb with Sn or Ge.[6, 8, 11] For example, mixing Pb and Sn on the B site has yielded devices with photoconversion efficiencies (PCEs) exceeding 20%.[35-39] Sn-containing perovskites have been widely studied, with PCEs approaching 15%,[40] whereas Ge-containing perovskites have been less well studied and show poorer performance.[41, 42] For Sn- and Ge-containing perovskites, the primary mechanism of degradation involves the oxidation of the B atom from divalent to tetravalent,[6, 16, 43-47] which disrupts the network of corner-sharing octahedra responsible for many dynamic processes.[48-52] Mixing Sn and Ge at the B-site has been shown to improve photovoltaic performance and stability compared to pure Pb-free compositions.[6, 11, 16, 45-47, 53] For example, $CsSn_{0.5}Ge_{0.5}I_3$ exhibits a PCE of 7% and improved stability relative to $CsGeI_3$ or $CsSnI_3$, through the formation of a passivating oxide layer.[45] A hybrid Sn-Ge perovskite with 5 mol% Ge gave a PCE of nearly 8%.[44] Efforts into understanding the formation and stability of Sn- and Ge-containing perovskites is desirable to continue to parse the structure-property relationships that govern material performance.

View Article Online
DOI: 10.1039/D6QI00612D

The relationships between processing conditions, composition, and properties of mixed Sn-Ge perovskites can be clarified by examining the structures through characterization techniques that probe both long-range order and local environments. Magnetic resonance techniques that distinguish the local chemical and electronic environments with atomic resolution are particularly suited to the study of perovskites and their wide-ranging dynamic phenomena. Solid-state nuclear magnetic resonance (NMR) spectroscopy has been applied to various perovskites,[54-59] providing information on substituents, phase segregation, and dynamics at the atomic scale, with each crystallographic site investigated using different reporter nuclei.[15, 23, 33, 34, 60-62] Perovskites containing appropriately accessible nuclei may be amenable to nuclear quadrupole resonance (NQR) spectroscopy, in which the quadrupolar interaction can be highly sensitive to small changes in local structure and defects.[58]

This study examines the solid-solution $CsSn_xGe_{1-x}Br_3$ and explores how their structures and optical properties are influenced by three preparative routes: solvent synthesis (SS), mechanochemical synthesis (MCS) by high-energy ball milling, and high-temperature (HT) solid-state reaction. The structures were evaluated by powder and single crystal X-ray diffraction (XRD) and by NMR (^{133}Cs, ^{119}Sn, ^{73}Ge) and NQR (^{81}Br) spectroscopy.

Results and Discussion

XRD, ^{133}Cs NMR spectra, and band gaps of $CsGeBr_3$, $CsSn_{0.5}Ge_{0.5}Br_3$, and $CsSnBr_3$

Contributing to previous examples of Sn-Ge perovskites,[16, 44-46, 53, 63] this work describes the solid solution $CsSn_xGe_{1-x}Br_3$ prepared as microcrystalline bulk powders. Because the synthetic method can influence structure and physical properties,[60, 62, 64, 65] samples of $CsGeBr_3$, $CsSn_{0.5}Ge_{0.5}Br_3$, and $CsSnBr_3$ were prepared in three ways (SS, MCS, and HT). They were characterized by XRD, NMR and NQR spectroscopy, with optical band gap measurements (Figure 1 and Table 1).

View Article Online
DOI: 10.1039/D6QI00612D

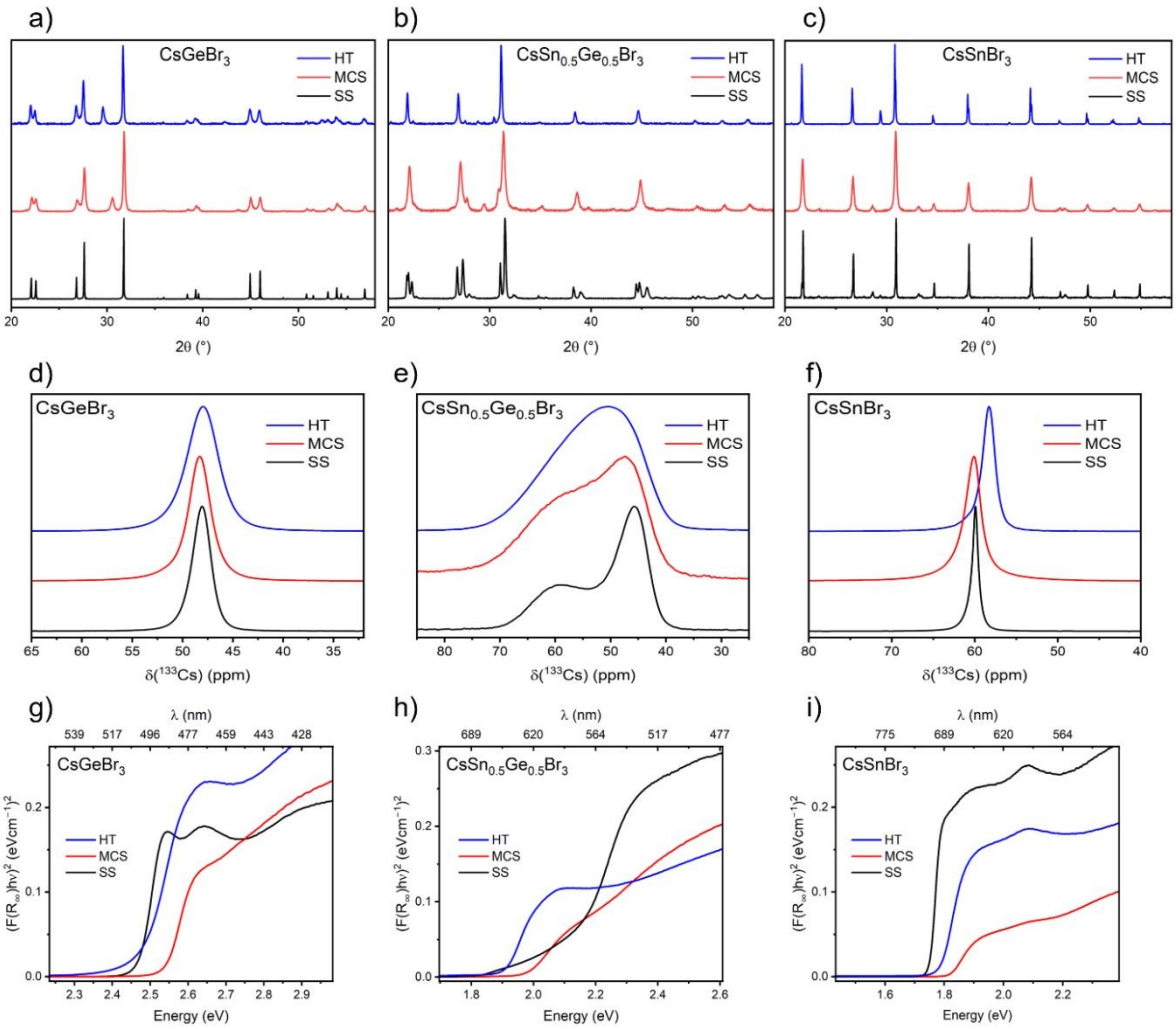

Figure 1. (a–c) Powder XRD patterns, (d–f) ^{133}Cs NMR spectra, and (g–i) diffuse reflectance spectra for $CsGeBr_3$, $CsSn_{0.5}Ge_{0.5}Br_3$, and $CsSnBr_3$ samples prepared via SS, MCS, and HT routes.

View Article Online
DOI: 10.1039/D6QI00612D

Table 1. Cell parameters, ^{133}Cs spin lattice relaxation times, ^{133}Cs NMR linewidths, and band gaps for $CsSn_xGe_{1-x}Br_3$ (x = 0, 0.50, 1) synthesized via SS, MCS, and HT routes.[a]

Sample	*a* (Å)	α (°)	T_1 (s)	FWHM (Hz)	Band gap (eV)
$CsGeBr_3$ (*R*3*m*)					
SS	5.6485	88.73	501	170	2.5
MCS	5.6505	88.84	112	240	2.5
HT	5.6469	88.85	254	290	2.5
$CsSn_{0.5}Ge_{0.5}Br_3$ (*R*3*m*)					
SS	5.6754	88.96	231	560	2.2
MCS	5.6624	89.53	—	—	—
HT	5.7458	89.43	—	—	—
$CsSn_{0.5}Ge_{0.5}Br_3$ ($Pm\bar{3}m$)					
SS	5.5010	90	32	870	1.8
MCS	5.7495	90	31	1450	2.0
HT	5.7391	90	51	1500	1.9
$CsSnBr_3$ ($Pm\bar{3}m$)					
SS	5.8035	90	33	65	1.8
MCS	5.8039	90	24	240	1.8
HT	5.8023	90	25	140	1.8

[a] Estimated errors are 0.0002 Å for *a*, 0.02° for α (except for 90°, which is exact), < 0.5 s for T_1, ±5-30 Hz for FWHM, and ±0.05 eV for band gap. The cell parameters for the trigonal structural models in *R*3*m* correspond to a primitive rhombohedral cell to facilitate comparison to the cubic model.

The powder XRD patterns confirm the presence of the expected phases (Figures 1a-c), whose relative amounts and cell parameters were extracted from Rietveld refinements (Figures S1–S3 and Tables S1–S2). The $CsGeBr_3$ samples contained a trigonal perovskite phase ($KBrO_3$-type, space group $R3m$), whose lower symmetry is evident by peak splitting, whereas the $CsSnBr_3$ samples possess a cubic phase ($CaTiO_3$-type, space group $Pm\bar{3}m$). On first inspection, the $CsSn_{0.5}Ge_{0.5}Br_3$ samples appeared to contain both phases in different amounts depending on the synthetic method: the trigonal and cubic phases were present in roughly equal proportions in the SS-prepared sample, whereas the cubic phase was more prevalent in the MCS- and HT-prepared samples. This observation suggests a miscibility gap between a Ge-rich trigonal phase and a Sn-rich cubic phase. However, the peak splitting originating from a trigonal distortion can be difficult to discern. It is possible to refine the patterns assuming that only a cubic phase is present for the intermediate members, especially for the MCS-prepared samples where the peaks are visibly broadened compared to the SS-prepared samples. All samples also contained small amounts of

View Article Online
DOI: 10.1039/D6QI00612D

other phases, such as $Cs_2(Ge,Sn)Br_6$, $Cs_4(Ge,Sn)Br_6$, $(Ge,Sn)Br_2$, CsBr, CsOH, and $(Ge,Sn)O_2$, which tended to increase upon exposure to air and moisture (relative humidity of ~60%) over 9 h during the data collection, implying that they are decomposition byproducts (Figures S1–S3 and Table S2). For comparison, thin films of the solid solution $CsSn_xGe_{1-x}Br_3$ have been previously fabricated by spray deposition, with a transition from trigonal to cubic structures indicated at x = 0.23.[53] Additional evidence would thus be helpful to ascertain whether the $CsSn_{0.5}Ge_{0.5}Br_3$ samples prepared here correspond to a single phase with the stated nominal composition, or a mixture of two phases with Ge- and Sn-rich compositions.

Initially, single crystals were sought within the MCS- and SS-prepared samples, but no suitably sized specimens could be found, which is unsurprising because these routes take place at room temperature or with fast precipitation. Instead, single crystals were found within the HT-prepared $CsGe_{0.5}Sn_{0.5}Br_3$ sample for structure determination. The crystals exhibited slightly different colours and morphology, so multiple crystals were selected for data collection. Structure refinements were guided by previous determinations of the end members: $CsGeBr_3$ crystallizes in the trigonal space group $R3m$ in which Ge-centred octahedra are slightly distorted because of the stereochemically active lone pair,[66] in contrast to $CsSnBr_3$ which adopts the ideal undistorted perovskite structure in the cubic space group $Pm\bar{3}m$. The results for two representative crystals of $CsGe_{0.5}Sn_{0.5}Br_3$ are presented, in which both trigonal and cubic models were considered (Tables S3–S5). The two models were essentially indistinguishable, as detailed in the Supporting Information, in terms of their agreement factors and their metrical details. For example, the bond angles around the tetrel atoms lie in the range of 88–92° in the trigonal model. An interpretation based on these results is that whatever distortions that Ge-centred octahedra may undergo locally, they would be masked by the disorder with Sn atoms centred within ideal octahedra. In common with other perovskite structures, the Br atoms experience slightly elevated displacement parameters relative to the other atoms, which may reflect the combined effects of slightly distorted Ge-centred octahedra and undistorted Sn-centred octahedra.

Cesium-133 is a receptive NMR probe nucleus (abundance = 100%, I = 7/2, γ = 3.5277 × 10^7 rad/T·s, Q = −0.34 fm^2) that is sensitive to changes in local symmetry introduced by site disorder in $CsSn_xGe_{1-x}Br_3$ (Figures 1d–f).[62, 65, 67, 68] The end members show a single resonance with an isotropic chemical shift δ_{iso} = 48 ppm for trigonal $CsGeBr_3$ and δ_{iso} = 60 ppm for cubic $CsSnBr_3$. For HT-prepared $CsSnBr_3$, the resonance shifts to slightly lower frequency, which has

View Article Online
DOI: 10.1039/D6QI00612D

been noted previously for samples prepared this way,[65] and correlates with shifts to higher frequency in the ^{119}Sn NMR and ^{81}Br NQR spectra. For all SS-prepared samples, the ^{133}Cs NMR resonance is narrower, which suggests greater ordering and fewer defects within the microcrystalline particles compared to samples prepared via MCS or HT methods. For all $CsSn_{0.5}Ge_{0.5}Br_3$ samples, the resonance spans over a range of 40–70 ppm, encompassing the region expected for the resonances for trigonal $CsGeBr_3$ and cubic $CsSnBr_3$. The ^{133}Cs NMR signal is broad and asymmetric for the HT $CsSn_{0.5}Ge_{0.5}Br_3$ sample, with more well-resolved shoulders appearing for the MCS sample, resolving into two peaks for the SS sample.

The ^{133}Cs longitudinal relaxation times (T_1) were measured using the saturation recovery method (Figures S4–S6 and Table 1). Their variation across samples reflects differences in crystallinity and defect concentrations depending on the synthetic route. For example, the decreasing T_1 values for $CsGeBr_3$ in the sequence of 501 s for SS, 254 s for HT, and 112 s for MCS routes suggest that the defect concentration increases in this order. The relaxation curves were fitted satisfactorily by a single-term exponential function for all samples except SS-prepared $CsSn_{0.5}Ge_{0.5}Br_3$, which required a biexponential function to model two sites, with the longer T_1 value assigned to a Ge-rich phase and the shorter T_1 assigned to a Sn-rich phase. Taken together, the asymmetric ^{133}Cs NMR line shapes and the fitting to two relaxation times for $CsSn_{0.5}Ge_{0.5}Br_3$ imply the occurrence of different Cs environments in $CsSn_{0.5}Ge_{0.5}Br_3$, due to phase segregation or domaining, as will be discussed later.

The diffuse reflectance spectra show absorption edges corresponding to band gaps of roughly 2.5 eV for $CsGeBr_3$, 1.8–2.2 eV for $CsSn_{0.5}Ge_{0.5}Br_3$, and 1.8 eV for $CsSnBr_3$, as extracted from Tauc plots (Figures 1g–i and S7–S9). For the end members $CsGeBr_3$ and $CsSnBr_3$, the band gaps for samples prepared by three alternate routes are consistent with previously reported values.[53, 67, 69] The band gaps for $CsSn_{0.5}Ge_{0.5}Br_3$ are intermediate between the end members, but they also show the widest discrepancies depending on the synthetic method. This likely stems from variations in *B*–*X* bond lengths and angles, which primarily control the magnitudes of band gaps in ABX_3 perovskites, depending on the preparation route. Of note, SS-prepared $CsSn_{0.5}Ge_{0.5}Br_3$ appears to show two edges in its diffuse reflectance spectrum, corresponding to band gaps of 1.8 and 2.2 eV, likely stemming from phase-segregated Sn- and Ge-rich compositions in the final product.

View Article Online
DOI: 10.1039/D6QI00612D

Morphology and elemental distribution of $CsGeBr_3$, $CsSn_{0.5}Ge_{0.5}Br_3$, and $CsSnBr_3$

Particle morphologies of the samples were examined by secondary electron micrographs (Figure 2). For the end members $CsGeBr_3$ and $CsSnBr_3$, the SS- and HT-prepared samples contained larger and well-defined particles compared to the MCS-prepared samples, which contained ill-defined particles with jagged edges over a wider size distribution resulting from impact shear forces occurring during ball-milling.[70, 71] EDX analyses showed chemical compositions in agreement with expectations (Figures S10–S22 and Table S6). For MCS- and HT-prepared $CsSn_{0.5}Ge_{0.5}Br_3$ samples, Sn and Ge were uniformly distributed at micron resolution. However, Sn- and Ge-rich regions were apparent in the SS-prepared sample of $CsSn_{0.5}Ge_{0.5}Br_3$ (Figure S11), as confirmed by an EDX line scan across a cluster showing two starkly distinct phases with compositions of roughly $CsSn_{0.2}Ge_{0.8}Br_3$ and $CsSn_{0.8}Ge_{0.2}Br_3$, with no intervening gradients (Figure 3).

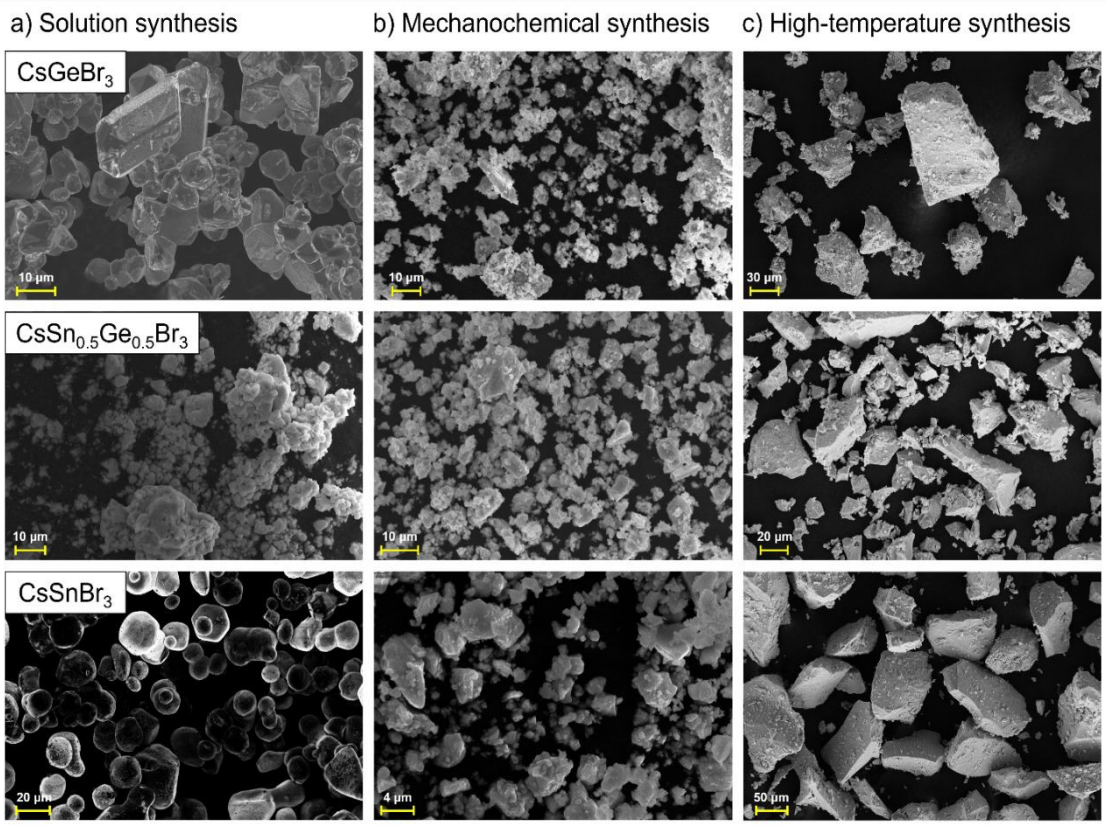

Figure 2. Secondary electron micrographs for (a) SS, (b) MCS, and (c) HT-prepared samples of $CsGeBr_3$, $CsSn_{0.5}Ge_{0.5}Br_3$, and $CsSnBr_3$.

View Article Online
DOI: 10.1039/D6QI00612D

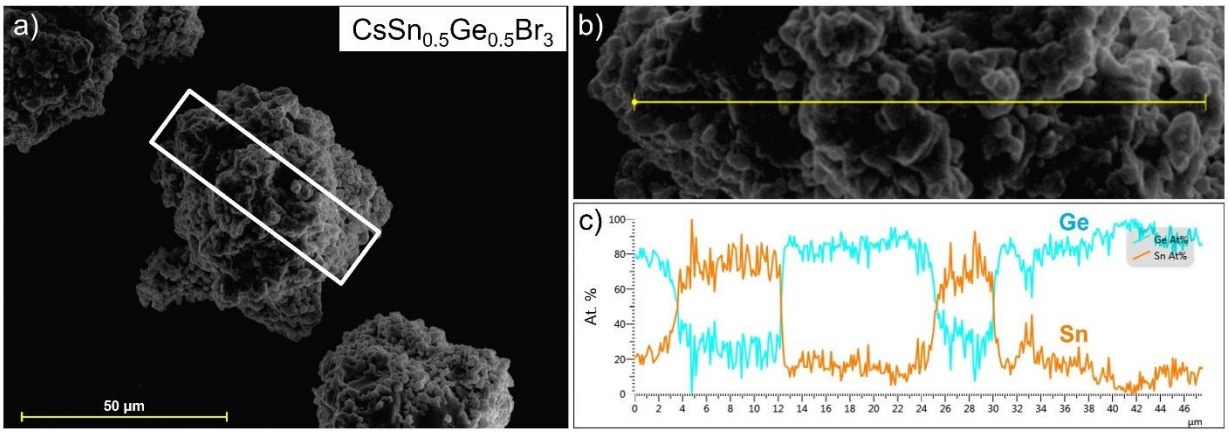

Figure 3. (a) Electron micrograph of SS-prepared $CsSn_{0.5}Ge_{0.5}Br_3$, with box outlining region of line scan. (b) Expanded view of region. (c) Atomic percents of Sn (orange) and Ge (teal).

^{73}Ge NMR of $CsGeBr_3$ and ^{119}Sn NMR of $CsSnBr_3$

The tetrel sites in the end members were examined by ^{73}Ge and ^{119}Sn NMR spectroscopy. Among various NMR-accessible nuclei, ^{73}Ge (7.76% abundance, I = 9/2, $\gamma = -0.9357 \times 10^7$ rad/T·s, $Q = -19.6$ fm^2) is one of the most challenging to study because of its low gyromagnetic ratio and natural abundance, with sensitivity issues further compounded by a moderate quadrupole moment.[72, 73] Even still, it offers direct access to the B-site in Ge-containing perovskites and its quadrupolar nature offers a sensitive means to examine local site symmetry.[67] The ^{73}Ge NMR spectra were collected for $CsGeBr_3$ (Figure 4) and the extracted parameters are compared with computed DFT values (Table 2) for the respective experimentally-refined SS, MCS, and HT crystal structures. The spectra for SS-, MCS-, and HT-prepared samples are similar (within error), implying that their structures have identical Ge environments regardless of synthetic pathway and agreeing with previous reports.[67] GIPAW-DFT-calculated ^{73}Ge C_Q values do not change significantly between the different input structures and are consistently overestimated by ~20%, as has been seen in earlier work.[67] Similarly, although the differences in the computed magnetic shieldings differ by ~13 ppm, this is within error of the experimental result across the three compounds. The spectrum of the MCS $CsGeBr_3$ sample shows a reduced signal-to-noise ratio, consistent with disorder and defects induced by mechanochemical shear forces, reducing nuclear spin-spin relaxation and leading to rapid decay of the NMR signal. Lastly, a small amount (5%) of residual $GeBr_4$,[74] present in (and an oxidation product of) the starting material, was also detected.

View Article Online
DOI: 10.1039/D6QI00612D

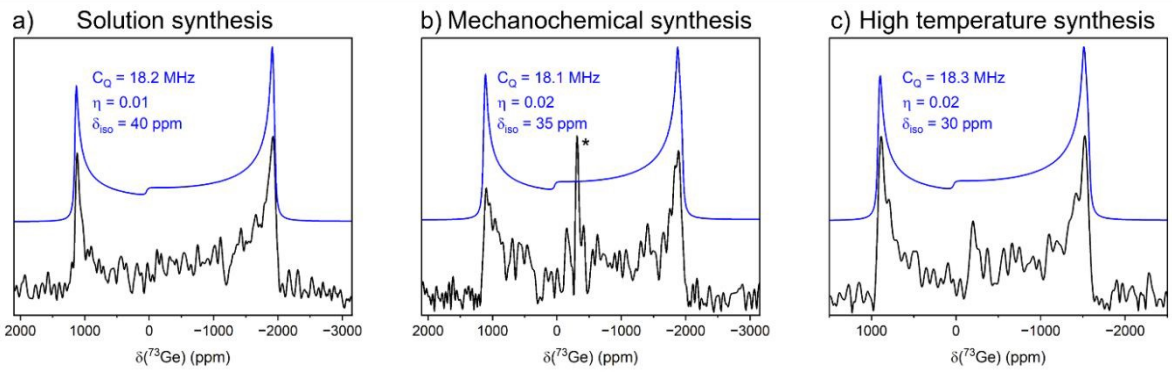

Figure 4. Non-spinning ^{73}Ge NMR spectra (experimental in black, fit in blue) at 18.8 T for (a) SS and (b) MCS, and at 21.1 T for (c) HT $CsGeBr_3$. The asterisk, *, marks a $GeBr_4$ impurity.

Table 2. Experimental and DFT-computed ^{73}Ge NMR parameters for $CsGeBr_3$ were prepared via SS, MCS, and HT routes.

	C_Q (MHz)		η		δ_{iso}(expt)/σ_{iso}(calc)		Ω (ppm) [a]		κ	
$CsGeBr_3$	expt	calc	expt	calc	expt	calc	expt	calc	expt	calc
SS	18.2(1)	22.30	0.01(1)	0.00	40(8)	1402.24	n.d.	29.61	n.d.	0.00
MCS	18.1(1)	23.10	0.02(1)	0.00	35(10)	1389.70	n.d.	31.78	n.d.	0.00
HT	18.3(1)	22.67	0.02(1)	0.00	30(12)	1398.57	n.d.	34.46	n.d.	0.00

[a] CSA was not determined (n.d.).

In contrast to the ^{73}Ge NMR spectra for $CsGeBr_3$, the chemical shifts in the ^{119}Sn NMR (8.59% abundance, $I = 1/2$, $\gamma = -10.0317 \times 10^7$ rad/T·s) spectra for $CsSnBr_3$ showed significant variation, spanning over 1000 ppm depending on the synthetic method (Figure 5). Peaks occur at –347 ppm for SS and –265 ppm for MCS samples, but at a higher frequency of 670 ppm for the HT sample. Their linewidths increase in the order of 19 kHz for SS, 39 kHz for MCS, and 57 kHz for HT samples, similar to previous reports indicating sensitivity to the synthetic method.[62, 65, 75] The line shapes are symmetric for the MCS and HT samples, but show tailing toward higher frequency for the SS sample, which matches an earlier report in which the authors attribute this shoulder to gradients in free-carrier concentration across solution-grown microcrystals.[75] To ensure no hidden resonances are present, the corresponding ^{119}Sn MAS NMR spectrum for SS $CsSnBr_3$ is shown in Figure S25, revealing no other degradation or impurity-related species.

View Article Online
DOI: 10.1039/D6QI00612D

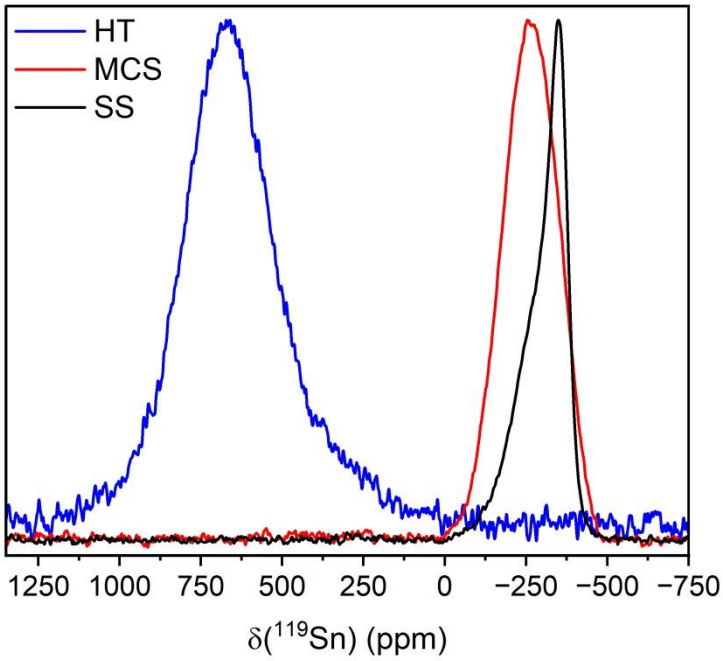

Figure 5. Non-spinning ^{119}Sn NMR spectra (11.7 T) for SS, MCS, and HT-prepared $CsSnBr_3$.

Previous reports for HT-synthesized $CsSnBr_3$ also showed that the ^{119}Sn NMR chemical shift appears at a higher frequency than SS and MCS samples, but not to the same extent as described here; the value depends strongly on the synthesis temperature and duration (e.g., from –289 to –179 ppm for samples prepared by similar methods).[62,65,75] The origin of this chemical shift dependence is unclear but it may arise from a combination of factors, including changes in the local Sn environment (including the expression of a stereochemically active lone pair), defect concentration, and sample degradation.[23, 62, 65, 75] The significant difference in chemical shift between the HT and SS or MCS samples is reminiscent of a Knight shift or paramagnetic interactions, which would not typically be expected for a diamagnetic sample such as $CsSnBr_3$. However, light-induced paramagnetic defects of Pb^{3+} and Pb^0 have recently been proposed to affect the NMR spectra of related lead halide perovskites.[76, 77] Similarly, paramagnetic Sn^{3+} centres have been observed in $SrSnO_3$,[78] as well as metallic Sn in degraded $MASnI_3$,[23] and most recently, the observation of a carrier-dependent Knight shift contribution to ^{119}Sn chemical shifts for $CsSnBr_3$.[75] To investigate the hypothesis that paramagnetic species could be responsible for the large chemical shift difference in HT $CsSnBr_3$, its EPR spectrum was collected (Figure S27). A signal was detected at an isotropic *g*-value of 2.003 ± 0.001, providing evidence of a paramagnetic

View Article Online
DOI: 10.1039/D6QI00612D

contribution. Unfortunately, the specific Sn speciation present or why this effect is so pronounced only in the HT sample remains unclear at this time.

^{81}Br NQR of $CsGeBr_3$ and $CsSnBr_3$

There has been renewed interest in applying NQR spectroscopy as a powerful tool for studying quadrupolar nuclei in various materials, including perovskites.[58, 79-88] Through the quadrupolar interaction mediated by the electric-field gradient (EFG) at the nucleus, NQR spectroscopy offers high sensitivity for probing local chemical environments and discerning subtle changes in site symmetry and disorder. The Br sites within the $CsGeBr_3$ and $CsSnBr_3$ samples were examined by their ^{81}Br (49.31% abundance, $I = 3/2$, $\gamma = 7.2498 \times 10^7$ rad/T·s, $Q = 26.15$ fm^2) NQR spectra (Figure 6). The SS samples exhibit much narrower linewidths than the MCS and HT samples, consistent with their higher degree of crystallinity and larger crystallites (Figure 2). In contrast, the MCS samples are known to contain smaller crystallites with more defects[60, 62, 89, 90] leading to wider EFG distributions and shorter nuclear spin-spin relaxation times, which cause spectral broadening. The spectra were fitted to extract NQR parameters (Figure S28), which were compared with DFT computed values (Table 3).

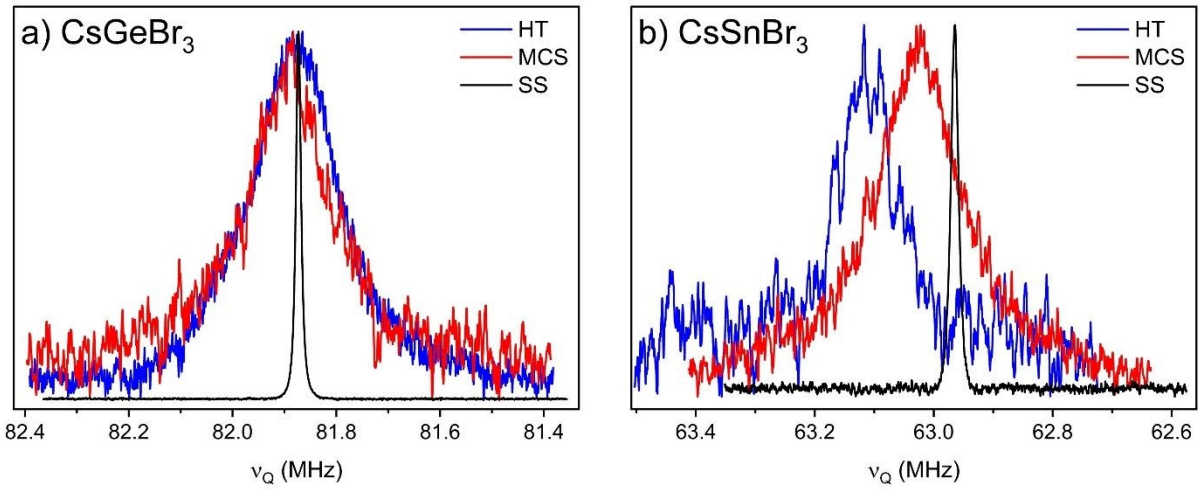

Figure 6. ^{81}Br NQR spectra for (a) $CsGeBr_3$ and (b) $CsSnBr_3$.

View Article Online
DOI: 10.1039/D6QI00612D

Table 3. Experimental and DFT computed ^{81}Br NMR and NQR parameters for $CsGeBr_3$ and $CsSnBr_3$ prepared via SS, MCS, and HT routes.

	NQR			NMR			
	$\|\nu_Q\|$ (MHz)		FWHM (kHz)	C_Q (MHz)		η	
Sample	expt	calc	Expt (±0.2)	expt [a]	calc	expt	calc
$CsGeBr_3$							
SS	81.873	91.30	11.4	163.746(1)	182.60	0.000(5)	0.00
MCS	81.884	90.70	180.6	163.775(10)	181.40	0.000(10)	0.01
HT	81.879	90.85	209.5	163.764(8)	181.70	0.000(10)	0.01
$CsSnBr_3$							
SS	62.957	73.85	19.2	125.933(2)	147.70	0.000(8)	0.00
MCS	63.025	73.85	225.4	126.057(10)	147.70	0.000(20)	0.00
HT	63.110	73.85	156.9	126.225(10)	147.70	0.000(15)	0.00

[a] Sign of C_Q could not be determined experimentally.

For both compounds, the SS samples always produce the lowest NQR frequency, ν_Q, consistent with high crystallinity. For $CsGeBr_3$, the quadrupole coupling constant, C_Q, does not depend on the synthetic method. For $CsSnBr_3$, the values vary considerably with the synthetic method, although the ν_Q values fall within typical ranges from the literature.[91] The larger C_Q value for the HT method further supports a more strained EFG, which may be induced from a larger lone-pair effect on Sn, while the overall paramagnetic species reduces the S/N of the spectrum due to fast relaxation. Comparing with DFT, similar to what is observed for ^{73}Ge, there is a systematic overestimation of the C_Q values for each input structure, while no significant change or trend can be observed from the ^{81}Br NMR parameters computed for either $CsGeBr_3$ or $CsSnBr_3$. Still, *a priori* estimation of the ν_Q values from DFT assist to define a range for experimental acquisition of the desired signal. Lastly, in conjunction with the discussion above about the varied ^{119}Sn NMR spectra of $CsSnBr_3$, synthetic treatments have been proposed to affect Br dynamics in tin halide perovskites,[62, 92] which can be significant enough to result in ionic conductivity at room temperature.[93]

MCS-synthesized solid solution $CsSn_xGe_{1-x}Br_3$

The XRD data for MCS and HT $CsSn_{0.5}Ge_{0.5}Br_3$ samples can be refined to both $R3m$ and $Pm\bar{3}m$ space groups, while exhibiting homogeneous B-site elemental distribution through EDX with broad ^{133}Cs NMR signals spanning the rhombohedral $CsGeBr_3$ and cubic $CsSnBr_3$ chemical shift ranges. These results demonstrate the ambiguity that can remain when only examining materials at either the local or extended length scales. The observation that SS $CsSn_{0.5}Ge_{0.5}Br_3$ is

View Article Online
DOI: 10.1039/D6QI00612D

a heterogeneous mixture of Sn- and Ge-rich compositions of roughly $CsSn_{0.2}Ge_{0.8}Br_3$ and $CsSn_{0.8}Ge_{0.2}Br_3$ from these same techniques further demonstrates that in all cases, there can be gradients in elemental distributions throughout a bulk sample. To further study the behaviour of B-site mixing in $CsSn_xGe_{1-x}Br_3$, a series of samples of varying composition were synthesized via MCS.

Additional members of the $CsSn_xGe_{1-x}Br_3$ series were prepared by MCS routes with nominal compositions at x = 0, 0.10, 0.25, 0.50, 0.75, 0.90, 1. Based on EDX of the resulting samples, the obtained phases had actual compositions of x = 0, 0.14, 0.28, 0.54, 0.66, 0.91, and 1 (Table S6 and Figures S13–S19). These samples were then examined by diffuse reflectance spectroscopy, Raman spectroscopy, ^{133}Cs and ^{119}Sn NMR spectroscopy, and powder XRD.

The diffuse reflectance spectra were converted to Tauc plots with the assumption of direct band gaps (Figures 7a and S8). The band gap decreases gradually from 2.5 to 1.8 eV with greater Sn substitution on proceeding from $CsGeBr_3$ to $CsSnBr_3$. The Raman spectra show major features corresponding to phonon scattering modes at 140 [$E^4{}_{TO}$], 162 [$A^3{}_{1TO}$], and 208 cm^{-1} [$A^3{}_{1LO}$] for $CsGeBr_3$, as assigned by Huang et al.,[94] and at 114 [$T^3_{1u}(TO)$] and 184 cm^{-1} [$T^3_{1u}(LO)$] for $CsSnBr_3$ (Figure 7b).[95] Greater Sn substitution generally shifts the Raman peaks to lower wavenumber.

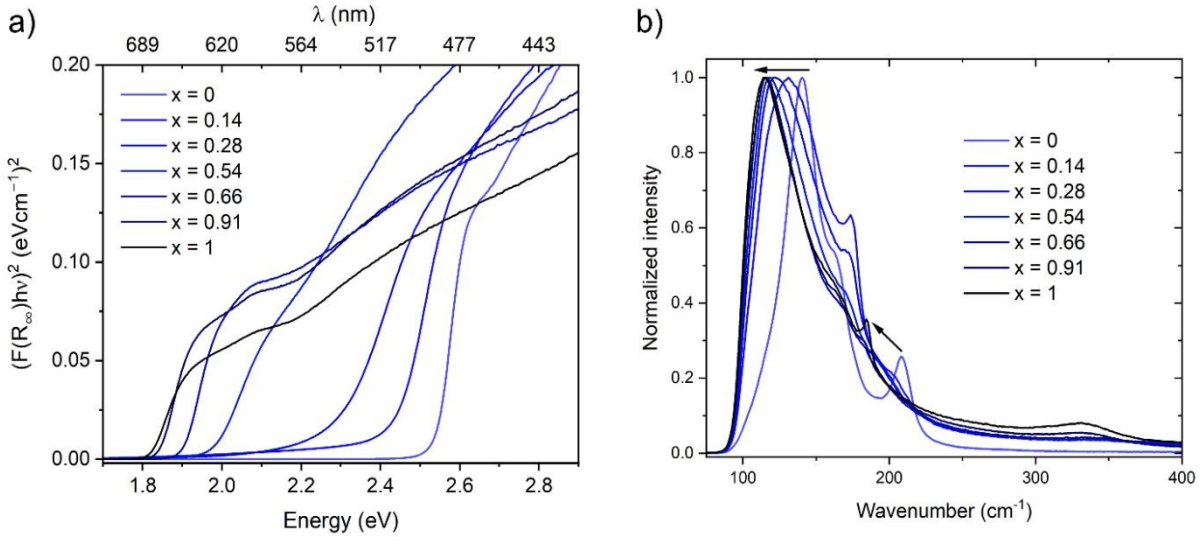

Figure 7. (a) Diffuse reflectance spectra converted to Tauc plots and (b) Raman spectra for $CsSn_xGe_{1-x}Br_3$.

As before, the ^{133}Cs NMR spectra show a single resonance with δ_{iso} of 48 ppm for trigonal $CsGeBr_3$ and 60 ppm for cubic $CsSnBr_3$ (Figure 8a and Table 4). As Sn substitutes for Ge in $CsGeBr_3$, the peak gradually shifts to lower frequency until x = 0.54, at which point the signal is

View Article Online
DOI: 10.1039/D6QI00612D

maximally broadened to encompass the high frequency region characteristic of the $Pm\bar{3}m$ $CsSnBr_3$. At higher Sn concentrations, only the high frequency peak centred at 60 ppm remains; it does not shift but only becomes gradually narrower. ^{133}Cs T_1 relaxation measurements were performed for the series (Figure S5), which begin at a maximum of 112 s for $CsGeBr_3$ and gradually shorten on proceeding to $CsSnBr_3$ (T_1 = 24 s). ^{119}Sn relaxation has been shown to be sensitive to Br^- dynamics in $CsSnBr_3$ and $MASnBr_3$.[62, 92] While MCS induces defects and generates nano/microcrystalline powders, which can decrease spin-lattice relaxation, the ^{133}Cs T_1 values are also influenced by the crystal structure and elemental composition. Specifically, the Ge-rich phases have longer relaxation times, suggesting that the Br^- rearrangement contributes to T_1 shortening when Sn is introduced into the structure. Thus, the interplay of elemental disorder, defect concentration, halogen rearrangement (if present) and structure all impact the spin-lattice relaxation and are difficult to disentangle in these solid-solutions.

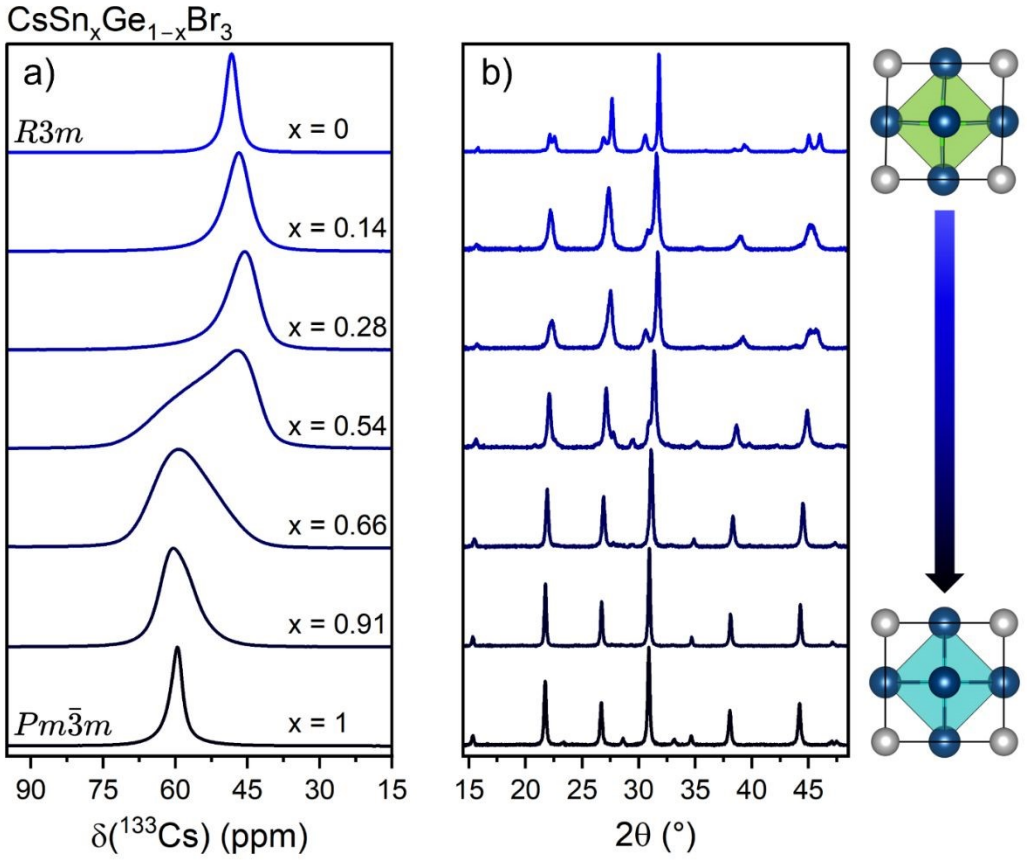

Figure 8. (a) ^{133}Cs NMR spectra and (b) powder XRD patterns for MCS $CsSn_xGe_{1-x}Br_3$ samples. Trigonal $CsGeBr_3$ shows a slight distortion (top) relative to cubic $CsSnBr_3$ (bottom).

View Article Online
DOI: 10.1039/D6QI00612D

Table 4. Cell parameters and ^{133}Cs NMR data for MCS-prepared $CsSn_xGe_{1-x}Br_3$.[a] Compositions as measured via EDX are used to constrain Rietveld refinements for analysis.

Sample	*a* (Å)	α (°)	δ_{iso} (ppm) ± 1	T_1 (s)	FWHM (Hz)	Band gap (eV)
$CsGeBr_3$ (*R*3*m*)	5.6505	88.84	48	112	240	2.5
$CsSn_{0.14}Ge_{0.86}Br_3$ (*R*3*m*)	5.6542	89.21	47	92	470	2.4
$CsSn_{0.28}Ge_{0.72}Br_3$ (*R*3*m*)	5.6662	89.37	46	70	590	2.3
$CsSn_{0.54}Ge_{0.46}Br_3$ (*R*3*m*)	5.6624	89.53	47	31	1450	2.0
$CsSn_{0.54}Ge_{0.46}Br_3$ ($Pm\bar{3}m$)	5.7495	90	57			
$CsSn_{0.66}Ge_{0.34}Br_3$ ($Pm\bar{3}m$)	5.7744	90	60	32	1180	1.9
$CsSn_{0.91}Ge_{0.09}Br_3$ ($Pm\bar{3}m$)	5.7960	90	61	22	640	1.8
$CsSnBr_3$ ($Pm\bar{3}m$)	5.8039	90	60	24	235	1.8

[a] Estimated errors are 0.0002 Å for *a*, 0.02° for α (except for 90°, which is exact), < 0.5 s for T_1, ± 5-30 Hz for FWHM, and ±0.05 eV for band gap. The cell parameters for the trigonal structural models in *R*3*m* correspond to a primitive rhombohedral cell to facilitate comparison to the cubic model.

The powder XRD patterns show that the splitting characteristic (e.g., diffraction peaks near 22° and 27° in 2θ) of the trigonal structure of $CsGeBr_3$ is no longer apparent even at x = 0.14 (Figure 8b). This splitting could well be obscured because the diffraction peaks are broadened as a result of the ball-milling processes, which typically impart significant defects and strain. Based on the NMR data, the samples were assumed to adopt the trigonal structure for x = 0–0.28, both trigonal and cubic structures at x = 0.54, and cubic structures beyond this point. For the Ge-rich samples, the cell angle α based on a primitive rhombohedral cell is very close to 90° (Table 4). For the Sn-rich samples with cubic structures, the cell length *a* is gradually lengthened on proceeding from the midpoint of the solid solution to the end member $CsSnBr_3$.

The tetrel site in $CsSn_xGe_{1-x}Br_3$ was probed by ^{119}Sn NMR spectroscopy. In contrast to the discussions above, here it is sensible to start with the end member $CsSnBr_3$ and examine the trends as Ge substitutes for Sn. In general, the NMR spectra consist of a broad, symmetric resonance that shifts slightly to lower frequency and exhibits a lower signal-to-noise ratio due to the reduced amount of Sn with greater Ge substitution (Figure 9). The only perceptible change occurs in

View Article Online
DOI: 10.1039/D6QI00612D

$CsSn_{0.91}Ge_{0.09}Br_3$, which shows a CSA-dominated line shape arising from interactions with the rare Ge-centred octahedron interrupting the network of Sn-centred octahedra. The presence of CSA in $CsSn_{0.91}Ge_{0.09}Br_3$ was confirmed by the complete disappearance of the CSA broadened line shape when acquired under MAS NMR (Figure S26). By virtue of the neighbouring Ge-centred octahedron, there is a deviation from axial symmetry around the Sn atom. If this model is accepted, the simulated CSA line shape has a span of $\Omega = 410\pm10$ ppm and a skew κ of -0.68 ± 3. No attempts were made to obtain ^{73}Ge NMR spectra due to the sensitivity associated with a large second-order quadrupolar line shape and the low [Ge] resulting from Sn substitution.

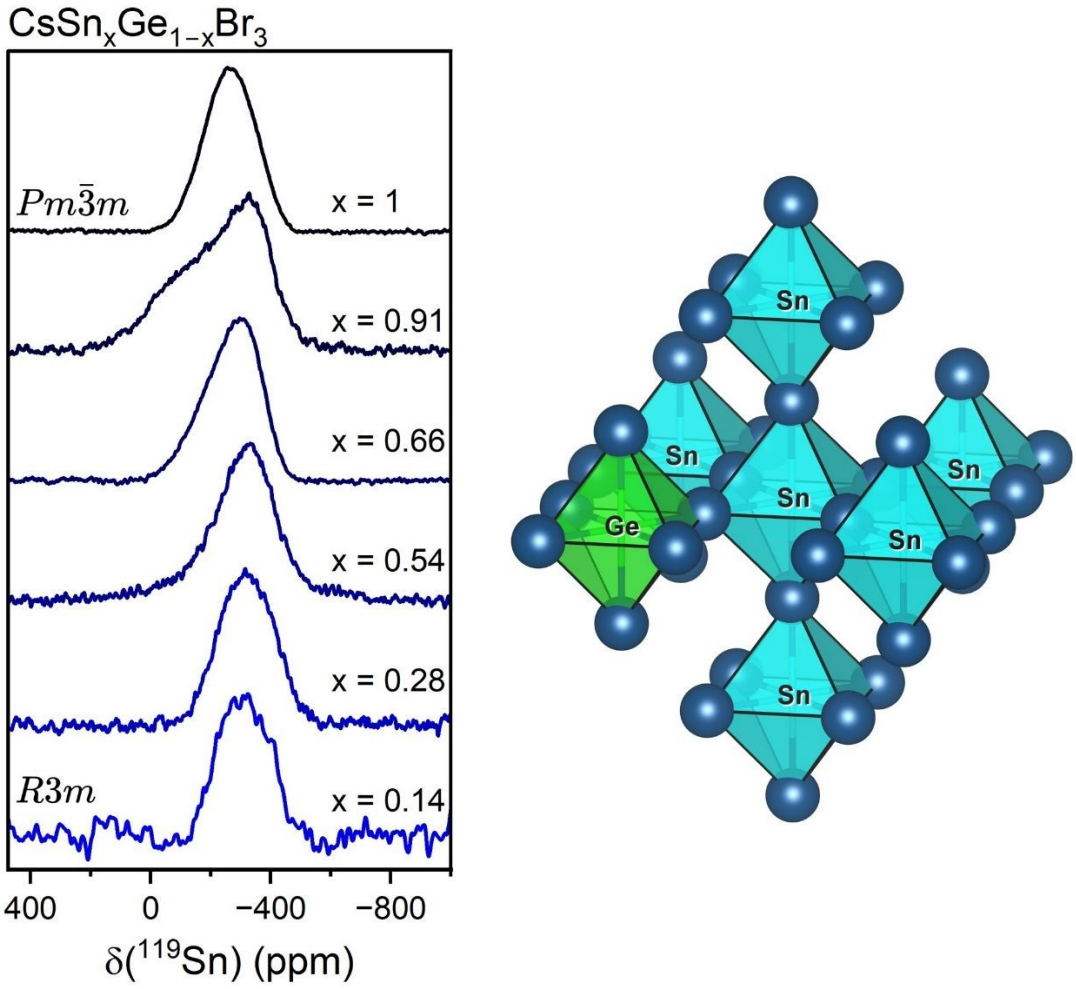

Figure 9. Non-spinning ^{119}Sn NMR spectra for $CsSn_xGe_{1-x}Br_3$ (left). Model for local environment of a Sn-centred octahedron with connectivity to symmetry-breaking Ge-centred octahedron in $CsSn_{0.91}Ge_{0.09}Br_3$ (right).

View Article Online
DOI: 10.1039/D6QI00612D

Trends in band gap, relaxation times, and structure

The results obtained up to this stage are now combined to identify general trends in how various properties of $CsSn_xGe_{1-x}Br_3$ depend on Sn content and synthetic method (Figure 10).

The band gaps appear to lie within two groups, with larger gaps for the Ge-rich trigonal phases and smaller ones for the Sn-rich cubic phases (Figure 10a). Within each group, the band gap decreases roughly linearly, as indicated by fits to linear equations for the MCS samples. The band gap is tuneable within these groups. The choice of synthetic method introduces variations in the band gap; for a given nominal composition, SS samples consistently exhibit smaller gaps by about 0.1 eV.

The ^{133}Cs spin-lattice relaxation times shorten considerably on proceeding from $CsGeBr_3$ to $CsSnBr_3$ (Figure 10b), consistent with previous proposals that Br rearrangements are much more pronounced in Sn-containing perovskites, including the end member $CsSnBr_3$.[62] The relaxation times are highly dependent on the synthetic method. The relaxation times are extremely long for the SS samples, implying better crystallinity, whereas they are always the shortest for the MCS samples, which consist of smaller, poorly formed particles with presumably greater defect concentrations.

Substituting Ge with larger Sn atoms is expected to expand the unit cell, but the cell parameters also appear to fall within two groups (Figure 10c). Based on the trends in the cell length a and the cell angle α, the discontinuity midway suggests a miscibility gap (estimated to be $0.4 < x < 0.6$) between the trigonal structure for Ge-rich samples and the cubic structure for Sn-rich samples. As the Sn content increases, the cell angle α mainly increases within the trigonal structure whereas the cell length a increases within the cubic structure. Similar to the trends in ^{133}Cs NMR relaxation times, the SS-prepared samples tend to be outliers, giving smaller unit cells than the HT and MCS samples.

Summarizing the diffraction, NMR, and microscopy results, the solvent synthesis approach is the most effective for producing highly crystalline solids, as it facilitates nucleation and allows large crystallites with well-defined morphologies to form. In contrast, the high energy shear forces from mechanochemical ball milling produce coarser materials with less directed morphology and a larger degree of structural variations of the local- and medium-range polyhedra. Likewise, MCS leads to crystal defects within the lattice. HT samples exist in the intermediate regime between SS and MCS, with improved crystallinity compared to MCS samples, but with the added complication

View Article Online
DOI: 10.1039/D6QI00612D

of the formation of a paramagnetic species in the pure Sn phase. The subtle changes in local structure, crystallinity, defects and paramagnetic species clearly influence the optical properties of these materials, but may have even greater consequence concerning the intrinsic ferroelectric properties of $CsGeBr_3$ (governed by the degree of Ge off-centring in $[GeBr_6]^{4-}$ octahedra), or the metallic/ionic conductivity reported for $CsSnBr_3$, and how the presence of Sn(III)/Sn(0) centres, or the Ge/Sn^{2+} active lone pair may influence these properties.

View Article Online
DOI: 10.1039/D6QI00612D

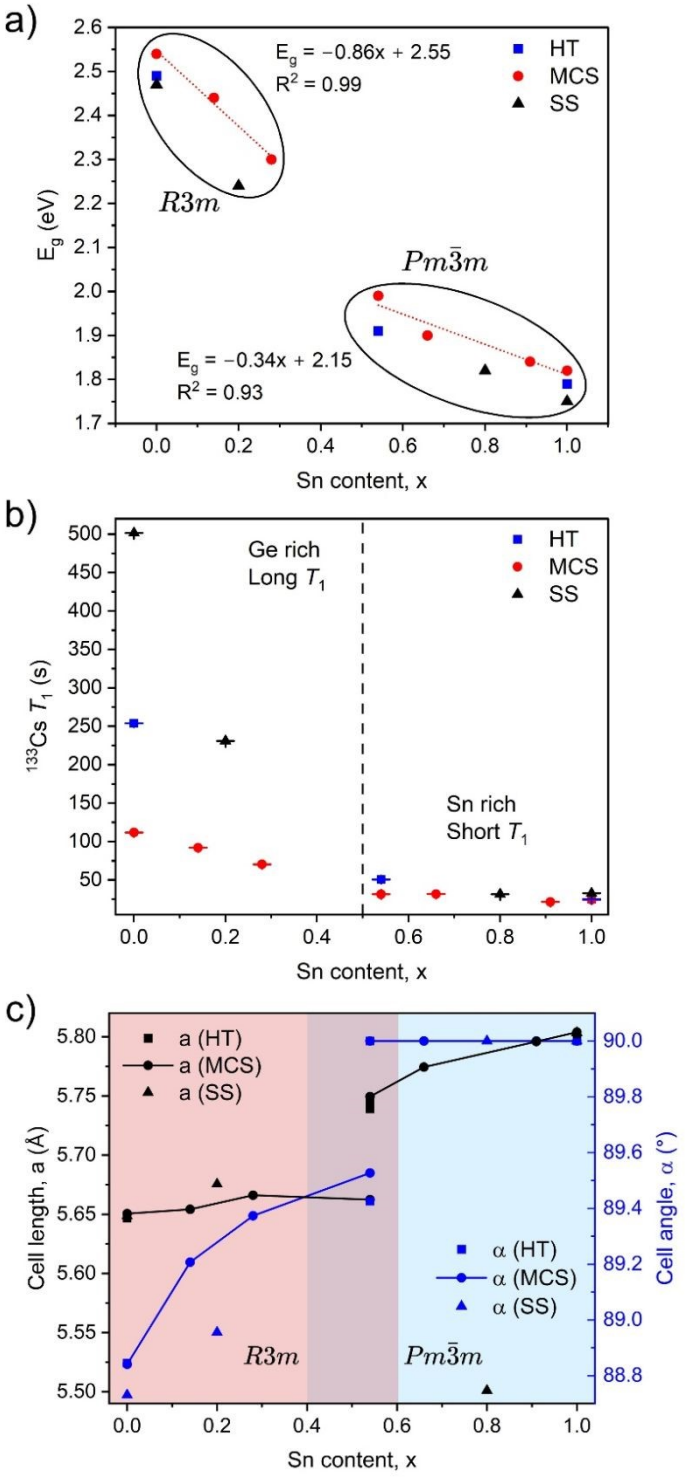

Figure 10. Trends in (a) band gaps, (b) ^{113}Cs relaxation times, and (c) cell parameters as a function of Sn content in $CsSn_xGe_{1-x}Br_3$ samples prepared by SS, MCS, and HT routes.

View Article Online
DOI: 10.1039/D6QI00612D

Conclusions

This study provides a comprehensive overview of the crucial aspects of material design for the $CsSn_xGe_{1-x}Br_3$ system. By combining diffraction methods and localized probing techniques, notably NMR and NQR spectroscopy, it has been determined that the optical characteristics of these lead-free perovskites are significantly influenced by the interplay between their composition and synthetic methodology. Understanding the phase space and the effects of differing processing conditions on a material is crucial for rational material design, with structure-property relationships governing all aspects of applications-guided material synthesis. The structural characterization reveals a composition-dependent phase transition, with a miscibility gap occurring near the 1:1 composition. The system transitions from a trigonal Ge-rich phase with distorted octahedra to a cubic Sn-rich phase, forming two distinct groups that correspond to these crystallographic phases, with adjustable optical band gaps following a linear dependence on x in each region rather than changing continuously. Solvent synthesis produces highly crystalline particles with low defect densities as shown by narrow NMR linewidths and long nuclear spin-lattice relaxation times but suffers from phase segregation in the Sn-Ge mixed case. In contrast, mechanochemical and high-temperature approaches improve macroscopic mixing of B-site cations but introduce significant lattice strain and more defects. This is especially evident in the high-temperature sample, where EPR spectroscopy reveals paramagnetic defects that may cause the substantial ^{119}Sn chemical shift changes observed. Further investigation of this complex compositional space with focus on applications-based performance and stability tests is essential since material homogeneity, structure, and optical properties vary with preparation method and composition. Characterization across multiple length scales is an essential component for these materials, particularly as site disorder and ion mixing complicate analysis using traditional methods.

Acknowledgements

The Natural Sciences and Engineering Research Council (NSERC) of Canada, the ATUMS training program, the CREATE program, the University of Alberta Faculties of Science and Graduate Studies, the Alberta Innovates Strategic Projects Program, and the Canada Research Chairs program are acknowledged for their generous research support. The Chemistry Centre Magnetic Resonance (C^2MR) Facility within the College of Natural and Applied Sciences is

View Article Online
DOI: 10.1039/D6QI00612D

supported by the Canada Foundation for Innovation (CFI), the Government of Alberta and the Faculty of Science (University of Alberta). R.W.H. acknowledges support from NSERC (CGSD3), Alberta Innovates (AIGSS), and the Government of Alberta (AGES). D.S. and C.N. acknowledge support from Alberta Innovates Graduate Student Scholarship. Access to the 21.1 T NMR spectrometer was provided by the National Ultrahigh-Field NMR Facility for Solids (Ottawa, ON), a national research facility funded by a consortium of Canadian universities and managed by the National Research Council Canada. The authors thank Dr. Victor V. Terskikh for assistance with the 900 MHz experiments (National Ultrahigh-Field NMR Facility for Solids).

View Article Online
DOI: 10.1039/D6QI00612D

References

(1) Kojima, A.; Teshima, K.; Shirai, Y.; Miyasaka, T. Organometal halide perovskites as visible-light sensitizers for photovoltaic cells. *J Am Chem Soc* **2009**, *131* (17), 6050-6051. DOI: 10.1021/ja809598r.
(2) Li, X.; Li, P.; Wu, Z.; Luo, D.; Yu, H.-Y.; Lu, Z.-H. Review and perspective of materials for flexible solar cells. *Materials Reports: Energy* **2021**, *1* (1), 100001-100001. DOI: https://doi.org/10.1016/j.matre.2020.09.001.
(3) Kim, J. Y.; Lee, J. W.; Jung, H. S.; Shin, H.; Park, N. G. High-Efficiency Perovskite Solar Cells. *Chem Rev* **2020**, *120* (15), 7867-7918. DOI: 10.1021/acs.chemrev.0c00107.
(4) Jena, A. K.; Kulkarni, A.; Miyasaka, T. Halide Perovskite Photovoltaics: Background, Status, and Future Prospects. *Chem Rev* **2019**, *119* (5), 3036-3103. DOI: 10.1021/acs.chemrev.8b00539.
(5) Xiao, Z.; Song, Z.; Yan, Y. From Lead Halide Perovskites to Lead-Free Metal Halide Perovskites and Perovskite Derivatives. *Adv Mater* **2019**, *31* (47), e1803792. DOI: 10.1002/adma.201803792.
(6) Xi, J.; Loi, M. A. The Fascinating Properties of Tin-Alloyed Halide Perovskites. *ACS Energy Lett* **2021**, *6* (5), 1803-1810. DOI: 10.1021/acsenergylett.1c00289.
(7) Kamat, P. V.; Kuno, M. Halide Ion Migration in Perovskite Nanocrystals and Nanostructures. *Accounts of Chemical Research* **2021**, *54* (3), 520-531. DOI: 10.1021/acs.accounts.0c00749.
(8) Ke, W.; Kanatzidis, M. G. Prospects for low-toxicity lead-free perovskite solar cells. *Nat Commun* **2019**, *10* (1), 965. DOI: 10.1038/s41467-019-08918-3.
(9) Almutlaq, J.; Yin, J.; Mohammed, O. F.; Bakr, O. M. The Benefit and Challenges of Zero-Dimensional Perovskites. *The Journal of Physical Chemistry Letters* **2018**, *9* (14), 4131-4138. DOI: 10.1021/acs.jpclett.8b00532.
(10) Ahmed, S.; Gondal, M. A.; Alzahrani, A. S.; Parvaz, M.; Ahmed, A.; Hussain, S. Recent Trends and Challenges in Lead-Free Perovskite Solar Cells: A Critical Review. *ACS Applied Energy Materials* **2024**, *7* (4), 1382-1397. DOI: 10.1021/acsaem.3c02327.
(11) Ke, W.; Stoumpos, C. C.; Kanatzidis, M. G. "Unleaded" Perovskites: Status Quo and Future Prospects of Tin-Based Perovskite Solar Cells. *Adv Mater* **2019**, *31* (47), e1803230. DOI: 10.1002/adma.201803230.
(12) Chen, J.; Yang, Y.; Dong, H.; Li, J.; Zhu, X.; Xu, J.; Pan, F.; Yuan, F.; Dai, J.; Jiao, B.; et al. Highly efficient and stable perovskite solar cells enabled by low-dimensional perovskitoids. *Science Advances* **2022**, *8* (4), eabk2722. DOI: doi:10.1126/sciadv.abk2722.
(13) Kent, G. T.; Zhuang, J.; Albanese, K. R.; Zohar, A.; Morgan, E.; Kallistova, A.; Kautzsch, L.; Mikhailovsky, A. A.; Vishnoi, P.; Seshadri, R.; et al. Hybrid Iodide Perovskites of Divalent Alkaline Earth and Lanthanide Elements. *Journal of the American Chemical Society* **2023**, *145* (50), 27850-27856. DOI: 10.1021/jacs.3c11494.
(14) Zhao, Y.; Yavuz, I.; Wang, M.; Weber, M. H.; Xu, M.; Lee, J.-H.; Tan, S.; Huang, T.; Meng, D.; Wang, R.; et al. Suppressing ion migration in metal halide perovskite via interstitial doping with a trace amount of multivalent cations. *Nature Materials* **2022**, *21* (12), 1396-1402. DOI: 10.1038/s41563-022-01390-3.
(15) Xu, T.; Xiang, W.; Kubicki, D. J.; Liu, Y.; Tress, W.; Liu, S. Simultaneous Lattice Engineering and Defect Control via Cadmium Incorporation for High-Performance Inorganic Perovskite Solar Cells. *Advanced Science* **2022**, *9* (36), 2204486. DOI: https://doi.org/10.1002/advs.202204486.
(16) Ito, N.; Kamarudin, M. A.; Hirotani, D.; Zhang, Y.; Shen, Q.; Ogomi, Y.; Iikubo, S.; Minemoto, T.; Yoshino, K.; Hayase, S. Mixed Sn-Ge Perovskite for Enhanced Perovskite Solar Cell Performance in Air. *J Phys Chem Lett* **2018**, *9* (7), 1682-1688. DOI: 10.1021/acs.jpclett.8b00275.

View Article Online
DOI: 10.1039/D6QI00612D

(17) Schileo, G.; Grancini, G. Lead or no lead? Availability, toxicity, sustainability and environmental impact of lead-free perovskite solar cells. *Journal of Materials Chemistry C* **2021**, *9* (1), 67-76. DOI: 10.1039/D0TC04552G.
(18) Tenuta, E.; Zheng, C.; Rubel, O. Thermodynamic origin of instability in hybrid halide perovskites. *Scientific Reports* **2016**, *6* (1), 37654. DOI: 10.1038/srep37654.
(19) Li, Z.; Yang, M.; Park, J.-S.; Wei, S.-H.; Berry, J. J.; Zhu, K. Stabilizing Perovskite Structures by Tuning Tolerance Factor: Formation of Formamidinium and Cesium Lead Iodide Solid-State Alloys. *Chemistry of Materials* **2016**, *28* (1), 284-292. DOI: 10.1021/acs.chemmater.5b04107.
(20) Askar, A. M.; Bernard, G. M.; Wiltshire, B.; Shankar, K.; Michaelis, V. K. Multinuclear Magnetic Resonance Tracking of Hydro, Thermal, and Hydrothermal Decomposition of $CH_3NH_3PbI_3$. *The Journal of Physical Chemistry C* **2017**, *121* (2), 1013-1024. DOI: 10.1021/acs.jpcc.6b10865.
(21) Zhao, J.; Deng, Y.; Wei, H.; Zheng, X.; Yu, Z.; Shao, Y.; Shield, J. E.; Huang, J. Strained hybrid perovskite thin films and their impact on the intrinsic stability of perovskite solar cells. *Science Advances* **2017**, *3* (11), eaao5616. DOI: doi:10.1126/sciadv.aao5616.
(22) Park, B.-w.; Seok, S. I. Intrinsic Instability of Inorganic–Organic Hybrid Halide Perovskite Materials. *Advanced Materials* **2019**, *31* (20), 1805337. DOI: https://doi.org/10.1002/adma.201805337.
(23) Ha, M.; Karmakar, A.; Bernard, G. M.; Basilio, E.; Krishnamurthy, A.; Askar, A. M.; Shankar, K.; Kroeker, S.; Michaelis, V. K. Phase Evolution in Methylammonium Tin Halide Perovskites with Variable Temperature Solid-State ^{119}Sn NMR Spectroscopy. *The Journal of Physical Chemistry C* **2020**, *124* (28), 15015-15027. DOI: 10.1021/acs.jpcc.0c03589.
(24) Schileo, G.; Grancini, G. Halide perovskites: current issues and new strategies to push material and device stability. *Journal of Physics: Energy* **2020**, *2* (2), 021005. DOI: 10.1088/2515-7655/ab6cc4.
(25) Otero-Martínez, C.; Fiuza-Maneiro, N.; Polavarapu, L. Enhancing the Intrinsic and Extrinsic Stability of Halide Perovskite Nanocrystals for Efficient and Durable Optoelectronics. *ACS Applied Materials & Interfaces* **2022**, *14* (30), 34291-34302. DOI: 10.1021/acsami.2c01822.
(26) Miah, M. H.; Rahman, M. B.; Nur-E-Alam, M.; Islam, M. A.; Shahinuzzaman, M.; Rahman, M. R.; Ullah, M. H.; Khandaker, M. U. Key degradation mechanisms of perovskite solar cells and strategies for enhanced stability: issues and prospects. *RSC Advances* **2025**, *15* (1), 628-654, 10.1039/D4RA07942F. DOI: 10.1039/D4RA07942F.
(27) Li, J.; Cao, H. L.; Jiao, W. B.; Wang, Q.; Wei, M.; Cantone, I.; Lu, J.; Abate, A. Biological impact of lead from halide perovskites reveals the risk of introducing a safe threshold. *Nat Commun* **2020**, *11* (1), 310. DOI: 10.1038/s41467-019-13910-y.
(28) Van Gompel, W. T. M.; Herckens, R.; Reekmans, G.; Ruttens, B.; D'Haen, J.; Adriaensens, P.; Lutsen, L.; Vanderzande, D. Degradation of the Formamidinium Cation and the Quantification of the Formamidinium–Methylammonium Ratio in Lead Iodide Hybrid Perovskites by Nuclear Magnetic Resonance Spectroscopy. *The Journal of Physical Chemistry C* **2018**, *122* (8), 4117-4124. DOI: 10.1021/acs.jpcc.7b09805.
(29) Lanzetta, L.; Webb, T.; Zibouche, N.; Liang, X.; Ding, D.; Min, G.; Westbrook, R. J. E.; Gaggio, B.; Macdonald, T. J.; Islam, M. S.; et al. Degradation mechanism of hybrid tin-based perovskite solar cells and the critical role of tin (IV) iodide. *Nature Communications* **2021**, *12* (1), 2853. DOI: 10.1038/s41467-021-22864-z.
(30) Yao, H.; Zhou, F.; Li, Z.; Ci, Z.; Ding, L.; Jin, Z. Strategies for Improving the Stability of Tin-Based Perovskite ($ASnX_3$) Solar Cells. *Adv Sci (Weinh)* **2020**, *7* (10), 1903540. DOI: 10.1002/advs.201903540.
(31) Wang, S.; Jiang, Y.; Juarez-Perez, Emilio J.; Ono, Luis K.; Qi, Y. Accelerated degradation of methylammonium lead iodide perovskites induced by exposure to iodine vapour. *Nature Energy* **2016**, *2* (1), 16195. DOI: 10.1038/nenergy.2016.195.

View Article Online
DOI: 10.1039/D6QI00612D

(32) Fabini, D. H.; Laurita, G.; Bechtel, J. S.; Stoumpos, C. C.; Evans, H. A.; Kontos, A. G.; Raptis, Y. S.; Falaras, P.; Van der Ven, A.; Kanatzidis, M. G.; et al. Dynamic Stereochemical Activity of the Sn^{2+} Lone Pair in Perovskite $CsSnBr_3$. *Journal of the American Chemical Society* **2016**, *138* (36), 11820-11832. DOI: 10.1021/jacs.6b06287.
(33) Kubicki, D. J.; Prochowicz, D.; Hofstetter, A.; Zakeeruddin, S. M.; Gratzel, M.; Emsley, L. Phase Segregation in Potassium-Doped Lead Halide Perovskites from ^{39}K Solid-State NMR at 21.1 T. *J Am Chem Soc* **2018**, *140* (23), 7232-7238. DOI: 10.1021/jacs.8b03191.
(34) Kubicki, D. J.; Prochowicz, D.; Hofstetter, A.; Zakeeruddin, S. M.; Gratzel, M.; Emsley, L. Phase Segregation in Cs-, Rb- and K-Doped Mixed-Cation $(MA)_x(FA)_{1-x}PbI_3$ Hybrid Perovskites from Solid-State NMR. *J Am Chem Soc* **2017**, *139* (40), 14173-14180. DOI: 10.1021/jacs.7b07223.
(35) Kapil, G.; Bessho, T.; Sanehira, Y.; Sahamir, S. R.; Chen, M.; Baranwal, A. K.; Liu, D.; Sono, Y.; Hirotani, D.; Nomura, D.; et al. Tin–Lead Perovskite Solar Cells Fabricated on Hole Selective Monolayers. *ACS Energy Letters* **2022**, *7* (3), 966-974. DOI: 10.1021/acsenergylett.1c02718.
(36) Hu, S.; Otsuka, K.; Murdey, R.; Nakamura, T.; Truong, M. A.; Yamada, T.; Handa, T.; Matsuda, K.; Nakano, K.; Sato, A.; et al. Optimized carrier extraction at interfaces for 23.6% efficient tin–lead perovskite solar cells. *Energy & Environmental Science* **2022**, *15* (5), 2096-2107, 10.1039/D2EE00288D. DOI: 10.1039/D2EE00288D.
(37) Tong, J.; Jiang, Q.; Ferguson, A. J.; Palmstrom, A. F.; Wang, X.; Hao, J.; Dunfield, S. P.; Louks, A. E.; Harvey, S. P.; Li, C.; et al. Carrier control in Sn–Pb perovskites via 2D cation engineering for all-perovskite tandem solar cells with improved efficiency and stability. *Nature Energy* **2022**, *7* (7), 642-651. DOI: 10.1038/s41560-022-01046-1.
(38) Jiang, X.; Li, C.; Wang, X.; Peng, C.; Jiang, H.; Bu, H.; Zhu, M.; Yin, H.; He, B.; Li, H.; et al. Multifunctional Regulation of Highly Orientated Tin–Lead Alloyed Perovskite Solar Cells. *ACS Energy Letters* **2023**, *8* (2), 1068-1075. DOI: 10.1021/acsenergylett.2c02576.
(39) Zhang, T.; Wang, F.; Chen, H.; Qian, F.; Li, J.; Zheng, H.; Yuan, S.; Peng, X.; Wang, Y.; Huang, J.; et al. Synchronized B-site alloying for high-efficiency inorganic tin–lead perovskite solar cells. *Applied Physics Reviews* **2023**, *10* (4). DOI: 10.1063/5.0162009 (acccessed 5/10/2024).
(40) Yu, B.-B.; Chen, Z.; Zhu, Y.; Wang, Y.; Han, B.; Chen, G.; Zhang, X.; Du, Z.; He, Z. Heterogeneous 2D/3D Tin-Halides Perovskite Solar Cells with Certified Conversion Efficiency Breaking 14%. *Advanced Materials* **2021**, *33* (36), 2102055. DOI: https://doi.org/10.1002/adma.202102055.
(41) Krishnamoorthy, T.; Ding, H.; Yan, C.; Leong, W. L.; Baikie, T.; Zhang, Z.; Sherburne, M.; Li, S.; Asta, M.; Mathews, N.; et al. Lead-free germanium iodide perovskite materials for photovoltaic applications. *Journal of Materials Chemistry A* **2015**, *3* (47), 23829-23832. DOI: 10.1039/C5TA05741H.
(42) Kopacic, I.; Friesenbichler, B.; Hoefler, S. F.; Kunert, B.; Plank, H.; Rath, T.; Trimmel, G. Enhanced Performance of Germanium Halide Perovskite Solar Cells through Compositional Engineering. *ACS Applied Energy Materials* **2018**, *1* (2), 343-347. DOI: 10.1021/acsaem.8b00007.
(43) Ju, M.-G.; Dai, J.; Ma, L.; Zeng, X. C. Lead-Free Mixed Tin and Germanium Perovskites for Photovoltaic Application. *Journal of the American Chemical Society* **2017**, *139* (23), 8038-8043. DOI: 10.1021/jacs.7b04219.
(44) Ng, C. H.; Nishimura, K.; Ito, N.; Hamada, K.; Hirotani, D.; Wang, Z.; Yang, F.; Iikubo, S.; Shen, Q.; Yoshino, K.; et al. Role of GeI_2 and SnF_2 additives for SnGe perovskite solar cells. *Nano Energy* **2019**, *58*, 130-137. DOI: https://doi.org/10.1016/j.nanoen.2019.01.026.
(45) Chen, M.; Ju, M. G.; Garces, H. F.; Carl, A. D.; Ono, L. K.; Hawash, Z.; Zhang, Y.; Shen, T.; Qi, Y.; Grimm, R. L.; et al. Highly stable and efficient all-inorganic lead-free perovskite solar cells with native-oxide passivation. *Nat Commun* **2019**, *10* (1), 16. DOI: 10.1038/s41467-018-07951-y.
(46) Liu, M.; Pasanen, H.; Ali-Löytty, H.; Hiltunen, A.; Lahtonen, K.; Qudsia, S.; Smått, J.-H.; Valden, M.; Tkachenko, N. V.; Vivo, P. B-Site Co-Alloying with Germanium Improves the

View Article Online
DOI: 10.1039/D6QI00612D

Efficiency and Stability of All-Inorganic Tin-Based Perovskite Nanocrystal Solar Cells. *Angewandte Chemie International Edition* **2020**, *59* (49), 22117-22125. DOI: https://doi.org/10.1002/anie.202008724.
(47) Zhou, Y.-Q.; Xu, J.; Liu, J.-B.; Liu, B.-X. Alloy engineering in mixed Sn–Ge perovskites for photovoltaic application. *Journal of Materials Chemistry A* **2021**, *9* (11), 6955-6961, 10.1039/D0TA11107D. DOI: 10.1039/D0TA11107D.
(48) Miyata, K.; Meggiolaro, D.; Trinh, M. T.; Joshi, P. P.; Mosconi, E.; Jones, S. C.; De Angelis, F.; Zhu, X.-Y. Large polarons in lead halide perovskites. *Science Advances* **2017**, *3* (8), e1701217. DOI: doi:10.1126/sciadv.1701217.
(49) Herz, L. M. Charge-Carrier Mobilities in Metal Halide Perovskites: Fundamental Mechanisms and Limits. *ACS Energy Letters* **2017**, *2* (7), 1539-1548. DOI: 10.1021/acsenergylett.7b00276.
(50) Zhang, Z.; Saparov, B. Charge carrier mobility of halide perovskite single crystals for ionizing radiation detection. *Applied Physics Letters* **2021**, *119* (3). DOI: 10.1063/5.0057411
(51) Zhao, B.-Q.; Li, Y.; Chen, X.-Y.; Han, Y.; Wei, S.-H.; Wu, K.; Zhang, X. Engineering Carrier Dynamics in Halide Perovskites by Dynamical Lattice Distortion. *Advanced Science* **2023**, *10* (33), 2300386. DOI: https://doi.org/10.1002/advs.202300386.
(52) Liang, X.; Klarbring, J.; Baldwin, W. J.; Li, Z.; Csányi, G.; Walsh, A. Structural Dynamics Descriptors for Metal Halide Perovskites. *The Journal of Physical Chemistry C* **2023**, *127* (38), 19141-19151. DOI: 10.1021/acs.jpcc.3c03377.
(53) Kama, A.; Tirosh, S.; Itzhak, A.; Ejgenberg, M.; Cahen, D. New Pb-Free Stable Sn–Ge Solid Solution Halide Perovskites Fabricated by Spray Deposition. *ACS Applied Energy Materials* **2022**, *5* (3), 3638-3646. DOI: 10.1021/acsaem.1c04115.
(54) Hooper, R. W.; Sarkar, D.; Michaelis, V. K. Bulk and nanoscale semiconducting materials: Structural advances using solid-state NMR spectroscopy. *Current Opinion in Colloid & Interface Science* **2022**, *62*, 101631. DOI: https://doi.org/10.1016/j.cocis.2022.101631.
(55) Kubicki, D. J.; Stranks, S. D.; Grey, C. P.; Emsley, L. NMR spectroscopy probes microstructure, dynamics and doping of metal halide perovskites. *Nature Reviews Chemistry* **2021**, *5* (9), 624-645. DOI: 10.1038/s41570-021-00309-x.
(56) Dahlman, C. J.; Kubicki, D. J.; Reddy, G. N. M. Interfaces in metal halide perovskites probed by solid-state NMR spectroscopy. *Journal of Materials Chemistry A* **2021**, *9* (35), 19206-19244. DOI: 10.1039/D1TA03572J.
(57) Bernard, G. M.; Karmakar, A.; Michaelis, V. K. Solid-state NMR Studies of Halide Perovskite Materials with Photoconversion Potential. In *Reference Module in Chemistry, Molecular Sciences and Chemical Engineering*, Elsevier, 2021.
(58) Piveteau, L.; Morad, V.; Kovalenko, M. V. Solid-State NMR and NQR Spectroscopy of Lead-Halide Perovskite Materials. *J Am Chem Soc* **2020**, *142* (46), 19413-19437. DOI: 10.1021/jacs.0c07338.
(59) Franssen, W. M. J.; Kentgens, A. P. M. Solid-state NMR of hybrid halide perovskites. *Solid State Nucl Magn Reson* **2019**, *100*, 36-44. DOI: 10.1016/j.ssnmr.2019.03.005.
(60) Karmakar, A.; Bhattacharya, A.; Bernard, G. M.; Mar, A.; Michaelis, V. K. Revealing the Local Sn and Pb Arrangements in $CsSn_xPb_{1-x}Br_3$ Perovskites with Solid-State NMR Spectroscopy. *ACS Materials Letters* **2021**, *3* (3), 261-267. DOI: 10.1021/acsmaterialslett.0c00596.
(61) Sarkar, D.; Hooper, R. W.; Karmakar, A.; Bhattacharya, A.; Pominov, A.; Terskikh, V. V.; Michaelis, V. K. Metal Halide Perovskite and Perovskite-like Materials through the Lens of Ultra-wideline $^{35/37}$Cl NMR Spectroscopy. *ACS Materials Letters* **2022**, *4* (7), 1255-1263. DOI: 10.1021/acsmaterialslett.2c00377.
(62) Karmakar, A.; Bhattacharya, A.; Sarkar, D.; Bernard, G. M.; Mar, A.; Michaelis, V. K. Influence of hidden halogen mobility on local structure of $CsSn(Cl_{1-x}Br_x)_3$ mixed-halide perovskites by solid-state NMR. *Chemical Science* **2021**, *12* (9), 3253-3263, 10.1039/D0SC05614F. DOI: 10.1039/D0SC05614F.

View Article Online
DOI: 10.1039/D6QI00612D

(63) Nagane, S.; Ghosh, D.; Hoye, R. L. Z.; Zhao, B.; Ahmad, S.; Walker, A. B.; Islam, M. S.; Ogale, S.; Sadhanala, A. Lead-Free Perovskite Semiconductors Based on Germanium–Tin Solid Solutions: Structural and Optoelectronic Properties. *The Journal of Physical Chemistry C* **2018**, *122* (11), 5940-5947. DOI: 10.1021/acs.jpcc.8b00480.
(64) Safdari, M.; Phuyal, D.; Philippe, B.; Svensson, P. H.; Butorin, S. M.; Kvashnina, K. O.; Rensmo, H.; Kloo, L.; Gardner, J. M. Impact of synthetic routes on the structural and physical properties of butyl-1,4-diammonium lead iodide semiconductors. *Journal of Materials Chemistry A* **2017**, *5* (23), 11730-11738, 10.1039/C6TA10123B. DOI: 10.1039/C6TA10123B.
(65) Chaudhary, M.; Karmakar, A.; Mishra, V.; Bhattacharya, A.; Mumbaraddi, D.; Mar, A.; Michaelis, V. K. Effect of aliovalent bismuth substitution on structure and optical properties of $CsSnBr_3$. *Communications Chemistry* **2023**, *6* (1), 75. DOI: 10.1038/s42004-023-00874-w.
(66) Schwarz, U.; Hillebrecht, H.; Kaupp, M.; Syassen, K.; von Schnering, H. G.; Thiele, G. Pressure-Induced Phase Transition in $CsGeBr_3$ Studied by X-Ray Diffraction and Raman Spectroscopy. *Journal of Solid State Chemistry* **1995**, *118* (1), 20-27. DOI: https://doi.org/10.1006/jssc.1995.1305.
(67) Hooper, R. W.; Ni, C.; Tkachuk, D. G.; He, Y.; Terskikh, V. V.; Veinot, J. G. C.; Michaelis, V. K. Exploring Structural Nuances in Germanium Halide Perovskites Using Solid-State ^{73}Ge and ^{133}Cs NMR Spectroscopy. *The Journal of Physical Chemistry Letters* **2022**, *13* (7), 1687-1696. DOI: 10.1021/acs.jpclett.1c04033.
(68) Aebli, M.; Kaul, C. J.; Yazdani, N.; Krieg, F.; Bernasconi, C.; Guggisberg, D.; Marczak, M.; Morad, V.; Piveteau, L.; Bodnarchuk, M. I.; et al. Disorder and Halide Distributions in Cesium Lead Halide Nanocrystals as Seen by Colloidal ^{133}Cs Nuclear Magnetic Resonance Spectroscopy. *Chemistry of Materials* **2024**, *36* (6), 2767-2775. DOI: 10.1021/acs.chemmater.3c02901.
(69) Peedikakkandy, L.; Bhargava, P. Composition dependent optical, structural and photoluminescence characteristics of cesium tin halide perovskites. *RSC Advances* **2016**, *6* (24), 19857-19860, 10.1039/C5RA22317B. DOI: 10.1039/C5RA22317B.
(70) Do, J.-L.; Friščić, T. Mechanochemistry: A Force of Synthesis. *ACS Central Science* **2017**, *3* (1), 13-19. DOI: 10.1021/acscentsci.6b00277.
(71) Bhuiyan, F. H.; Li, Y.-S.; Kim, S. H.; Martini, A. Shear-activation of mechanochemical reactions through molecular deformation. *Scientific Reports* **2024**, *14* (1), 2992. DOI: 10.1038/s41598-024-53254-2.
(72) Michaelis, V. K.; Kroeker, S. ^{73}Ge Solid-State NMR of Germanium Oxide Materials: Experimental and Theoretical Studies. *The Journal of Physical Chemistry C* **2010**, *114* (49), 21736-21744. DOI: 10.1021/jp1071082.
(73) Michaelis, V. K.; Aguiar, P. M.; Terskikh, V. V.; Kroeker, S. Germanium-73 NMR of amorphous and crystalline GeO_2. *Chem Commun (Camb)* **2009**, (31), 4660-4662. DOI: 10.1039/b906642j.
(74) Greer, B. J.; Michaelis, V. K.; Terskikh, V. V.; Kroeker, S. Reconnaissance of diverse structural and electronic environments in germanium halides by solid-state ^{73}Ge NMR and quantum chemical calculations. *Canadian Journal of Chemistry* **2011**, *89* (9), 1118-1129. DOI: 10.1139/v11-052.
(75) Fabini, D. H.; Honasoge, K.; Cohen, A.; Bette, S.; McCall, K. M.; Stoumpos, C. C.; Klenner, S.; Zipkat, M.; Hoang, L. P.; Nuss, J.; et al. Noncollinear Electric Dipoles in a Polar Chiral Phase of $CsSnBr_3$ Perovskite. *Journal of the American Chemical Society* **2024**, *146* (23), 15701-15717. DOI: 10.1021/jacs.4c00679.
(76) Mishra, A.; Hope, M. A.; Emsley, L. Light-Induced Metallic and Paramagnetic Defects in Halide Perovskites from Magnetic Resonance. *ACS Energy Letters* **2024**, *9* (10), 5074-5080. DOI: 10.1021/acsenergylett.4c02557.
(77) Colella, S.; Todaro, M.; Masi, S.; Listorti, A.; Altamura, D.; Caliandro, R.; Giannini, C.; Carignani, E.; Geppi, M.; Meggiolaro, D.; et al. Light-Induced Formation of Pb^{3+} Paramagnetic

View Article Online
DOI: 10.1039/D6QI00612D

Species in Lead Halide Perovskites. *ACS Energy Letters* **2018**, *3* (8), 1840-1847. DOI: 10.1021/acsenergylett.8b00944.
(78) Silva, A.; Hurdley, F.; de Oliveira, A. L. M.; Slater, T.; da Silva Maia, A.; Folli, A.; dos Santos, I. M. G. An EPR investigation on reduced Sn centres in $SrSnO_3$ perovskite. *Materials Letters* **2024**, *368*, 136705. DOI: https://doi.org/10.1016/j.matlet.2024.136705.
(79) Hooper, R. W.; Lin, K.; Veinot, J. G. C.; Michaelis, V. K. 3D to 0D cesium lead bromide: A $^{79/81}$Br NMR, NQR and theoretical investigation. *Journal of Magnetic Resonance* **2023**, *352*, 107472. DOI: https://doi.org/10.1016/j.jmr.2023.107472.
(80) Piveteau, L.; Aebli, M.; Yazdani, N.; Millen, M.; Korosec, L.; Krieg, F.; Benin, B. M.; Morad, V.; Piveteau, C.; Shiroka, T.; et al. Bulk and Nanocrystalline Cesium Lead-Halide Perovskites as Seen by Halide Magnetic Resonance. *ACS Cent Sci* **2020**, *6* (7), 1138-1149. DOI: 10.1021/acscentsci.0c00587.
(81) Doherty, T. A. S.; Nagane, S.; Kubicki, D. J.; Jung, Y.-K.; Johnstone, D. N.; Iqbal, A. N.; Guo, D.; Frohna, K.; Danaie, M.; Tennyson, E. M.; et al. Stabilized tilted-octahedra halide perovskites inhibit local formation of performance-limiting phases. *Science* **2021**, *374* (6575), 1598-1605. DOI: doi:10.1126/science.abl4890.
(82) Aebli, M.; Porenta, N.; Aregger, N.; Kovalenko, M. V. Local Structure of Multinary Hybrid Lead Halide Perovskites Investigated by Nuclear Quadrupole Resonance Spectroscopy. *Chemistry of Materials* **2021**, *33* (17), 6965-6973. DOI: 10.1021/acs.chemmater.1c01945.
(83) Senocrate, A.; Moudrakovski, I.; Kim, G. Y.; Yang, T.-Y.; Gregori, G.; Grätzel, M.; Maier, J. The Nature of Ion Conduction in Methylammonium Lead Iodide: A Multimethod Approach. *Angewandte Chemie International Edition* **2017**, *56* (27), 7755-7759. DOI: https://doi.org/10.1002/anie.201701724.
(84) Mozur, E. M.; Hope, M. A.; Trowbridge, J. C.; Halat, D. M.; Daemen, L. L.; Maughan, A. E.; Prisk, T. R.; Grey, C. P.; Neilson, J. R. Cesium Substitution Disrupts Concerted Cation Dynamics in Formamidinium Hybrid Perovskites. *Chemistry of Materials* **2020**, *32* (14), 6266-6277. DOI: 10.1021/acs.chemmater.0c01862.
(85) Senocrate, A.; Moudrakovski, I.; Maier, J. Short-range ion dynamics in methylammonium lead iodide by multinuclear solid state NMR and ^{127}I NQR. *Physical Chemistry Chemical Physics* **2018**, *20* (30), 20043-20055, 10.1039/C8CP01535J. DOI: 10.1039/C8CP01535J.
(86) Franssen, W. M. J.; van Es, S. G. D.; Dervişoğlu, R.; de Wijs, G. A.; Kentgens, A. P. M. Symmetry, Dynamics, and Defects in Methylammonium Lead Halide Perovskites. *The Journal of Physical Chemistry Letters* **2017**, *8* (1), 61-66. DOI: 10.1021/acs.jpclett.6b02542.
(87) Scarperi, A.; Landi, N.; Costamagna, M.; Taddei, M.; Carignani, E.; Geppi, M.; Borsacchi, S. Probing Photoinduced Halide Segregation in $CH_3NH_3Pb(Br_xI_{1-x})_3$ Perovskites via in Situ Nuclear Quadrupole Resonance Spectroscopy. *Journal of the American Chemical Society* **2025**, *147* (37), 33799-33811. DOI: 10.1021/jacs.5c10094.
(88) Quarti, C.; Gautier, R.; Zacharias, M.; Gansmuller, A.; Katan, C. Nuclear Quadrupolar Resonance Structural Characterization of Halide Perovskites and Perovskitoids: A Roadmap from Electronic Structure Calculations for Lead–Iodide-Based Compounds. *Journal of the American Chemical Society* **2025**, *147* (1), 278-291. DOI: 10.1021/jacs.4c09877.
(89) Karmakar, A.; Askar, A. M.; Bernard, G. M.; Terskikh, V. V.; Ha, M.; Patel, S.; Shankar, K.; Michaelis, V. K. Mechanochemical Synthesis of Methylammonium Lead Mixed–Halide Perovskites: Unraveling the Solid-Solution Behavior Using Solid-State NMR. *Chemistry of Materials* **2018**, *30* (7), 2309-2321. DOI: 10.1021/acs.chemmater.7b05209.
(90) Karmakar, A.; Bernard, G. M.; Meldrum, A.; Oliynyk, A. O.; Michaelis, V. K. Tailorable Indirect to Direct Band-Gap Double Perovskites with Bright White-Light Emission: Decoding Chemical Structure Using Solid-State NMR. *J Am Chem Soc* **2020**, *142* (24), 10780-10793. DOI: 10.1021/jacs.0c02198.

View Article Online
DOI: 10.1039/D6QI00612D

(91) Yamada, K.; Nose, S.; Umehara, T.; Okuda, T.; Ichiba, S. ^{81}Br NQR and ^{119}Sn Mössbauer Study for $MSnBr_3$ (M = Cs and CH_3NH_3). *Bulletin of the Chemical Society of Japan* **2006**, *61* (12), 4265-4268. DOI: 10.1246/bcsj.61.4265
(92) Kubicki, D. J.; Prochowicz, D.; Salager, E.; Rakhmatullin, A.; Grey, C. P.; Emsley, L.; Stranks, S. D. Local Structure and Dynamics in Methylammonium, Formamidinium, and Cesium Tin(II) Mixed-Halide Perovskites from ^{119}Sn Solid-State NMR. *J Am Chem Soc* **2020**, *142* (17), 7813-7826. DOI: 10.1021/jacs.0c00647.
(93) Yamada, K.; Kawaguchi, H.; Matsui, T.; Okuda, T.; Ichiba, S. Structural Phase Transition and Electrical Conductivity of the Perovskite $CH_3NH_3Sn_{1-x}Pb_xBr_3$ and $CsSnBr_3$. *Bulletin of the Chemical Society of Japan* **2006**, *63* (9), 2521-2525. DOI: 10.1246/bcsj.63.2521
(94) Huang, L.-y.; Lambrecht, W. R. L. Vibrational spectra and nonlinear optical coefficients of rhombohedral $CsGeX_3$ halide compounds with X = I, Br, Cl. *Physical Review B* **2016**, *94* (11), 115202. DOI: 10.1103/PhysRevB.94.115202.
(95) Huang, L.-y.; Lambrecht, W. R. L. Lattice dynamics in perovskite halides $CsSnX_3$ with X = I, Br, Cl. *Physical Review B* **2014**, *90* (19), 195201. DOI: 10.1103/PhysRevB.90.195201.

View Article Online
DOI: 10.1039/D6QI00612D

The supporting data are provided in the Supplementary Information. Supplementary information includes X-ray diffraction, solid-state NMR spectroscopy, diffuse reflectance, electron microscopy and energy dispersive X-ray spectroscopy. Further experimental details, see DOI: [URL – format https://doi.org/DOI].